Analyzing of Cloud Macroscopic Characteristics in the Shigatse Area of the Tibetan Plateau Using the Total-Sky Images

JUN YANG, WEITAO LYU, AND YING MA

State Key Laboratory of Severe Weather, Chinese Academy of Meteorological Sciences, Beijing, China

YIJUN ZHANG

Institute of Atmospheric Sciences, Fudan University, and Shanghai Institute of Pollution Control and Ecological Security, Shanghai, China

QINGYONG LI

Beijing Key Laboratory of Transportation Data Analysis and Mining, Beijing Jiaotong University, Beijing, China

WEN YAO AND TIANSHU LU

State Key Laboratory of Severe Weather, Chinese Academy of Meteorological Sciences, Beijing, China

(Manuscript received 9 April 2018, in final form 24 June 2018)

ABSTRACT

The macroscopic characteristics of clouds in the Tibetan Plateau are crucial to understanding the local climatic conditions and their impact on the global climate and water vapor cycle. In this study, the variations of cloud cover and cloud types are analyzed by using total-sky images of two consecutive years in Shigatse, Tibetan Plateau. The results show that the cloud cover in Shigatse presents a distinct seasonal difference that is characterized by low cloud cover in autumn and winter and high cloud cover in summer and spring. July is the month with the largest cloud coverage, and its average cloud cover exceeds 75%. The probability of clouds in the sky is the lowest in November, with an average cloud cover of less than 20%. The diurnal variations of cloud cover in different months also have considerable differences. Specifically, cloud cover is higher in the afternoon than that in the morning in most months, whereas the cloud cover throughout the day varies little from July to September. The dominant cloud types in different months are also not the same. The proportion of clear sky is large in autumn and winter. Stratiform cloud occupies the highest percentage in March, April, July, and August. The probability of emergence of cirrus is highest in May and June. The Shigatse region has clear rainy and dry seasons, and correlation analysis between precipitation and clouds shows that the largest cumulative precipitation, the highest cloud cover, and the highest proportion of stratiform clouds occur simultaneously in July.

1. Introduction

Clouds play a vital role in the global (Stephens 2005) and regional (Garrett and Zhao 2006) radiation budget and climate feedbacks. However, cloud properties from observations still have large uncertainties for both microphysical properties (Zhao et al. 2012) and macrophysical properties. Because of its unique geographical features, the Tibetan Plateau (TiP) has a major influence on both local climate change and global atmospheric circulation. Knowledge of the cloud properties, and even the macroscopic properties such as cloud cover and cloud type, over the TiP is scarce and highly needed. Early studies on clouds of the TiP mainly depend on limited station observations, and most sites have only four measurements per day. Several studies have reported on temporal and spatial variations of the total cloud cover in the TiP using these subjective observations at weather stations (You et al. 2014; Duan and Wu 2006; Zhang et al. 2008). With the expeditious development of remote sensing technology, the application of satellite data has led to great progress in the analysis of precipitation and cloud characteristics, which provided knowledge about the large-area cloud properties

Corresponding author: Jun Yang, yangjun@cma.gov.cn

DOI: 10.1175/JAMC-D-18-0095.1

over the TiP (Li et al. 2006; Huang et al. 2007; Wang et al. 2016; Li and Zhang 2016). The results of satellite analysis showed that the TiP region has significant climatic diversity, and the cloud particles in the air have a completely different distribution in the different regions of the TiP. Specifically, the peak of cloud particles appeared in summer over the central and western region of the TiP, whereas in the eastern region the cloud particles in summer are even fewer than in spring and autumn (Wang et al. 2015). The observations derived from the MODIS satellite show that water vapor values and high clouds over the TiP also presented obvious seasonal variations, and the maximum and minimum of the average high cloud reflectance appeared in April and November, respectively (Gao et al. 2003). The joint observations from *CloudSat* and *CALIPSO* can even give the fine structure of clouds in the vertical direction (Luo et al. 2011). Overall, although satellite data provide a feasible solution for large-range cloud observations, our understanding of complex cloud water processes is still limited, which leads to great uncertainty in satellite inversion. Active ground-based observational equipment also provides a good means to retrieval the macro- and microphysical characteristics of clouds, and a comprehensive cloud observation was carried out at Nagqu of the TiP using cloud radar, ceilometer, and lidar (Liu et al. 2015; Song et al. 2017; Zhao et al. 2016, 2017). These active devices have also shown great advantages in cloud detection, especially in obtaining the vertical structure of the clouds. However, the results of both satellite and radar measurements need to be validated by ground-truth observations.

Total-sky imaging is a ''what you see is what you get'' observation scheme that provides an effective solution for analyzing the macroscopic features of the clouds. A number of total-sky-imaging instruments have been developed for different research purposes, such as the whole-sky imager (WSI; Johnson et al. 1988; Shields et al. 2013); the total-sky imager (TSI; Long and DeLuisi 1998); the all-sky imager (ASI; Huo and Lu 2009); the whole-sky camera (WSC; Calbó and Sabburg 2008); the total-sky cloud imager (TCI; Yang et al. 2012); the automatic-capturing digital fisheye camera (ADFC; Yamashita and Yoshimura 2012); the University of California, San Diego, sky imager (USI; Yang et al. 2014); the all-sky infrared visible analyzer (ASIVA; Klebe et al. 2014); and the Laboratoire Procédés Matériaux et Énergie Solaire (PROMES) sky imager (Chauvin et al. 2015). In addition, several commercial hemispherical imaging devices are publicly available, such as the TSI-880, SRF-02, ASI-16, PSV-100, and AllSky 340, manufactured by Yankee Environmental Systems, EKO Instruments, Schreder CMS, Prede Co., Ltd., and Diffraction Limited, respectively. All of the above devices can acquire color hemispherical images at specified time intervals in the daytime automatically. Using these hemispherical images, plenty cloud detection and classification algorithms have been proposed (Long et al. 2006; Souza-Echer et al. 2006; Heinle et al. 2010; Neto et al. 2010; Long 2010; Li et al. 2011; Kazantzidis et al.,2012; Ghonima et al. 2012; Yang et al. 2015; Chauvin et al. 2015; Yang et al. 2016).

Long-term continuous observation using a total-sky-imaging device in a certain area is an effective means of analyzing the macroscopic characteristics of the clouds in that region. Kazantzidis et al. (2012) conducted a 2-yr continuous field observation using their own total-sky-imaging equipment at the Aristotle University of Thessaloniki, Greece. Alonso et al. (2014) captured about 3 years of hemispherical images using a commercial TSI-880 device at the University of Almería in Spain. Yabuki et al. (2014) collected more than 2 years of whole-sky images using a PSV-100 all-sky camera system at Ny-Ålesund, Svalbard, Norway. Most of these field observations are just for obtaining a large number of total-sky images to study algorithms for cloud detection and classification. Huo and Lu (2012) compared the cloud covers of their ASI devices with the artificial observational records of the meteorological stations at three sites in China, and the total correlation coefficient between them can reach 0.77 for all cases. The commercial TSI instruments were widely applied in several atmospheric radiation measurement sites to host field campaigns routinely in the United States. However, there are still few reports of long-term ground-based cloud observations in the TiP. Using our self-developed TCI device, we carried out a 2-yr continuous field observation experiment in the Shigatse area of the TiP and analyzed the cloud macroscopic characteristics in that area. Section 2 describes the TCI instrument and the corresponding algorithms for cloud detection and cloud-type classification. The cloud macroscopic characteristics in the Shigatse area are presented in section 3. Section 4 gives a conclusion and proposals for future work.

2. Instrument and algorithms

The Chinese Academy of Meteorological Sciences designed and manufactured a total-sky cloud-image system mainly for automatic observations of cloud cover and cloud type. The kernel assembly unit of the TCI device consists of an industrial camera and a fisheye lens (field of view is 185°) that can automatically capture hemispherical color images with an imaging range of 1392 × 1024 pixels at a fixed time interval. To analyze the cloud macroscopic characteristics in the TiP, we installed a TCI device in the Shigatse area (29.25°N,

88.88°E), which is located in the southwest of the TiP, and conducted a 2-yr continuous cloud field observation from August 2012 to July 2014. During this field observation period, the TCI instrument can acquire a hemispherical image every 5 min in the daytime, and the effective range of the image is a circular region of 800 pixels in diameter after removing most of the ground objects and the surrounding invalid areas.

The cloud detection algorithm is the key technology to obtain accurate cloud-cover information from a total-sky image. Recently, Yang et al. (2017) proposed a differencing and threshold combination algorithm (DTCA) to detect clouds from the total-sky images acquired in the Shigatse area. In the DTCA algorithm, a channel operation was first applied to remove the uneven sky background due to the differences in atmospheric scattering, then the real clear-sky background differencing method or a single threshold algorithm is chosen for cloud detection depending on different sun occlusion conditions. Yang et al. (2017) quantitatively assessed the accuracy of the DTCA algorithm in estimating cloud fraction for different cloud types and different sun occlusions, which shows that the DTCA algorithm is superior to several traditional cloud detection methods, and its average cloud recognition error rate is only 5.2%. Although the joint observations from *CloudSat* and *CALIPSO* can give a precise vertical structure of clouds, which will provide a good reference for cloud-cover estimation and cloud-type recognition, the time resolution of these sensors makes it hard to meet the needs of real-time observation of total-sky images. Next, we will evaluate the DTCA algorithm in more detail using 100 different types of total-sky images. Considering that detecting clouds from a total-sky image is in fact a binary classification problem, each pixel in the image has only the following four possible classification cases (Yang et al. 2012): true positive (TP), true negative (TN), false positive (FP), and false negative (FN); TP means a pixel is cloud and the detection method also identifies the pixel as cloud, and FN denotes a pixel is cloud but the detection method incorrectly classifies the pixel as sky. Similarly, TN means a pixel is sky and the detection algorithm also classifies the pixel as sky, and FP denotes a pixel is sky but the detection method identifies the pixel as cloud. Here, we adopt the following two indicators to evaluate the performance of the DTCA algorithm:

$$\text{Precision} = \frac{\text{TP}}{\text{TP} + \text{FN}} \quad \text{and} \tag{1}$$

$$\text{Accuracy} = \frac{\text{TP} + \text{TN}}{\text{TP} + \text{FP} + \text{TN} + \text{FN}}. \tag{2}$$

The precision represents the extent to which clouds in the total-sky image are correctly detected, and the accuracy takes into account the correct identification of cloud and noncloud pixels, indicating the overall detection accuracy. For a good cloud detection algorithm, both indicators should be high. The standard cloud masks of 100 images are artificially interpreted by several experienced cloud observers as ground-truth observation of clouds in each total-sky image. Then, the precision and accuracy indexes for an image can be obtained by pixel-by-pixel comparison of the DTCA result with the standard cloud mask. Figure 1 denotes the specific precision and accuracy information of 100 total-sky images. The precision distribution of 100 sample images shows that most of the samples are more accurate than 90% but that there are still some samples with a precision of only about 80%. This is because these sample images contain a lot of thin clouds or cirrus clouds, and the existing cloud detection algorithms still have a low recognition accuracy for these clouds. Overall, however, the average precision of the DTCA algorithm can reach 95.8%, and the average accuracy is 94.0%. The evaluation results show that the accuracy of the DTCA algorithm is sufficient to ensure high-precision cloud-cover estimation.

Because of the lack of a unified cloud-classification standard and the low accuracy of classification methods, the cloud-type classification for the total-sky image is still a huge challenge. Using the total-sky cloud images obtained in Shigatse, we established a total-sky cloud image set (TCIS), in which the total-sky images contain five different sky types: clear sky, cumuliform, stratiform, cirriform, and mixed clouds. The first four types of images include only a single sky type, and the mixed clouds refer to an image that contains multiple cloud types. Note also that the stratiform type here includes not only stratiform cloud images but also the images of the sky covered with cumulonimbus clouds because it is hard to completely distinguish the two cloud types from a single visible image. There are a total of 5000 total-sky images in the TCIS, and each sky type contains 1000 images. Using this image set, Li et al. (2016) developed a cloud-type identification algorithm that is based on a set of microstructures that considered each total-sky cloud image as a set of microstructures rather than a collection of traditional pixels and obtained an average classification accuracy of 90.9%. Zhang (2017) proposed a transfer-learning training method for limited sample data and realized the application of the convolutional architecture for fast feature embedding ("Caffe") deep-learning framework (Jia et al. 2014) in the classification of total-sky cloud images. In this paper, we adopted the trained network parameters and deep-learning model provided by Zhang to perform cloud-type classification. The entire TCIS image set is used to

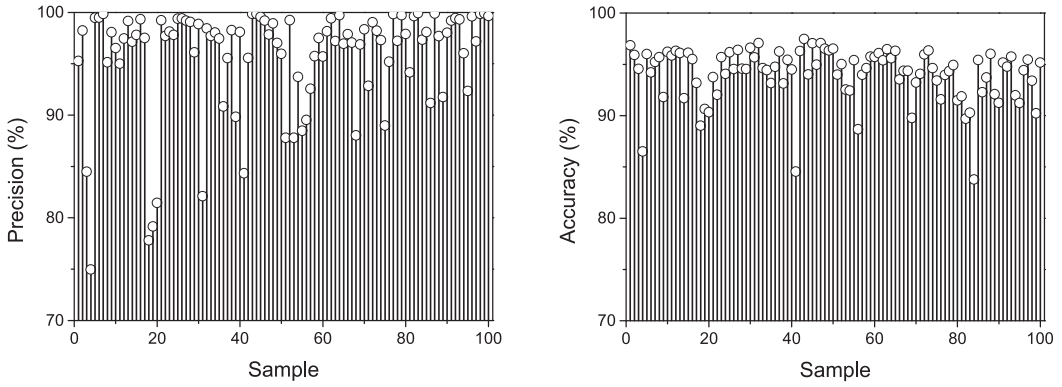

FIG. 1. The specific precision and accuracy information of 100 total-sky images.

assess the classification accuracy, and Table 1 shows the confusion matrix of the classification results. According to Table 1, both clear sky and stratiform clouds are relatively easy to identify, and their classification accuracy reaches 100%. The recognition of cirriform cloud is the most difficult, with an accuracy of 85.2%, and many cirriform clouds are mistakenly classified as clear sky because of their similar image features. In addition, the classification accuracies of cumuliform and mixed clouds are 94.3% and 94.7%, respectively. The average classification accuracy is 94.8%, which is higher than the state-of-the-art cloud-type classification algorithms.

3. Cloud macroscopic characteristics in Shigatse

The accuracies of the DTCA cloud detection algorithm and Caffe deep-learning cloud-type classification method have been evaluated in the previous section. Then, the cloud-cover and cloud-type information for each image can be obtained by using these algorithms to perform cloud detection and cloud classification on 2-yr continuous total-sky images in Shigatse. By counting the cloud-cover and cloud-type information of each image, we can get the statistical characteristics, such as monthly variation and diurnal variation of cloud cover and cloud type. The traditional Northern Hemisphere seasonal division method is adopted here. Namely, March, April, and May are spring; June, July, and August are summer; September, October, and November are autumn; and December, January, and February are winter. At the same site, there is a national ground weather station for real-time acquisition of several meteorological elements, such as temperature, pressure, relative humidity, and precipitation. We also analyze the changes of cloud cover and cloud type and their correlations with surface precipitation by combining the hourly observational data of the ground weather station in Shigatse.

a. Variation of cloud cover in Shigatse

The average cloud cover for a month can be obtained by averaging all cloud covers of that month. Figure 2 represents the monthly variation of cloud cover in Shigatse, which shows a clear seasonal distribution. Here, cloud amount is expressed as a percentage, where 100% represents that the entire sky is covered by clouds and 0% means completely clear sky. Generally, the amount of the clouds in winter and autumn is low, while the cloud cover in summer and spring is high. The seasonal distribution of cloud cover in Shigatse is closely related to local climate characteristics. The highest cloud cover occurred in July; the average cloud cover of that month was above 75%. The lowest cloud cover appeared in November, and the average cloud cover was below 20%.

In Shigatse's observational experiments, total-sky images were acquired continuously at 5-min intervals in the daytime, so we averaged the cloud covers at the same time of each day, yielding diurnal variations of cloud cover. In general, the daily radiation budget of the

TABLE 1. Confusion matrix of Caffe deep-learning classification.

	Clear sky	Cirriform	Cumuliform	Stratiform	Mixed clouds
Clear sky	1000	0	0	0	0
Cirriform	126	852	1	8	13
Cumuliform	0	3	943	31	23
Stratiform	0	0	0	1000	0
Mixed clouds	16	12	1	24	947

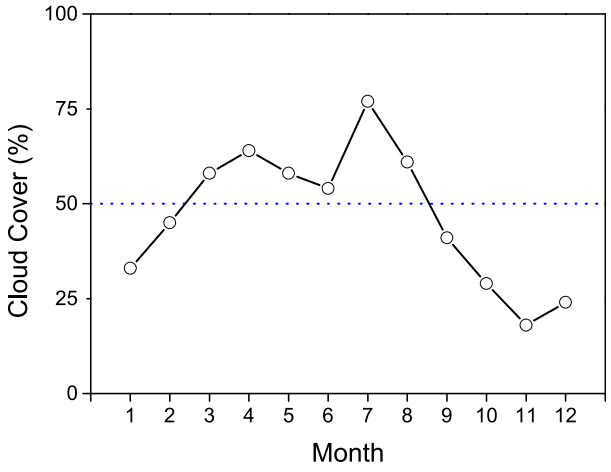

FIG. 2. Monthly variation of cloud cover in Shigatse.

land influences the change of cloud cover. With the increase of sunshine in the afternoon, convective activities have been strengthened and the amount of clouds has also increased significantly. Figure 3 shows the diurnal variation of cloud cover in Shigatse by monthly statistics. All of the times that appear in this study are China standard time (CST). From the time of cloud-cover appearance, the cloud cover was significantly higher in the afternoon than that in the morning for most months. However, from July to September, this trend is not obvious, and the difference of cloud covers between the morning and afternoon is not so large. This may be influenced by the southwest monsoon in the Indian Ocean (Shankar et al. 2002), and the steady stream of warm and humid airflow affects the cloudiness of Shigatse. Specifically, the cloud cover in July was about 75% all day, whereas the cloud-cover percentages in August and September were about 60% and 40%, respectively.

b. Variation of cloud type in Shigatse

Using trained network parameters and the Caffe deep-learning model, each total-sky image can be divided into one of clear sky, cumuliform, stratiform, cirriform, and mixed clouds. We have calculated the proportion of various cloud types on a monthly basis, and the results are shown in Fig. 4. It is clear that the proportion of clear sky in January exceeded 70%, and that the proportion of clear sky in November and December could reach even up to 90%. Although the proportion of clear sky in February and October was only about 40%, it still accounted for the largest proportion in those two months. The clouds in February and

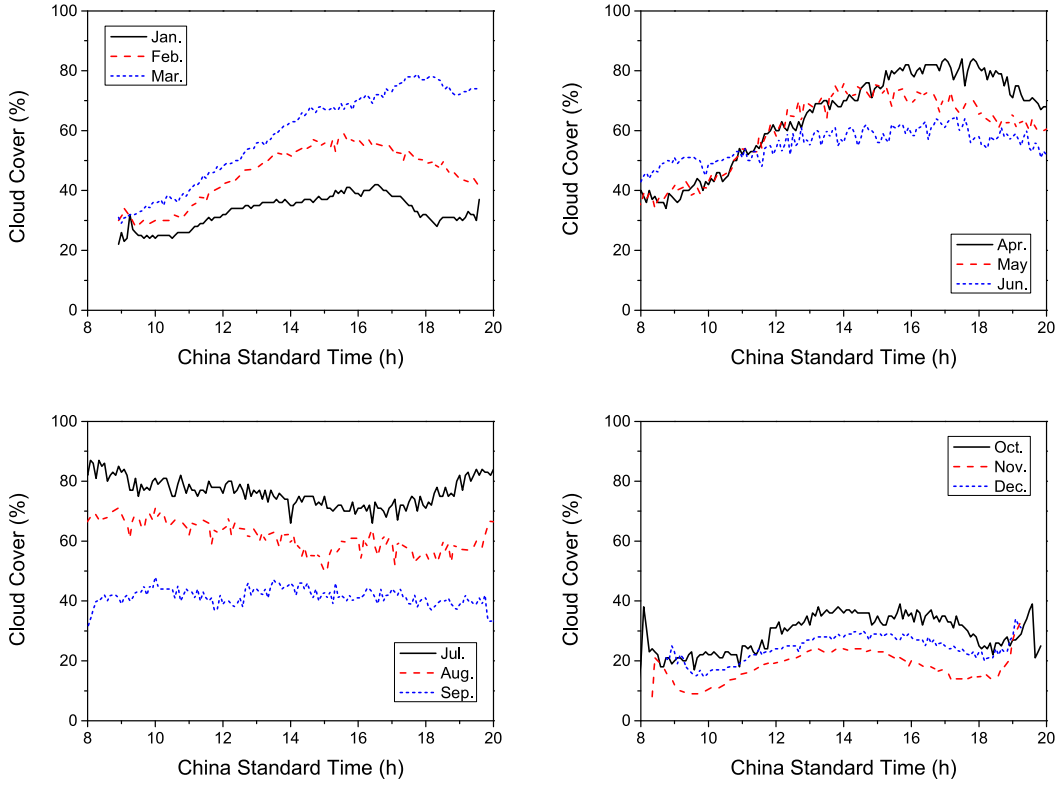

FIG. 3. Diurnal variation of cloud cover in Shigatse by month.

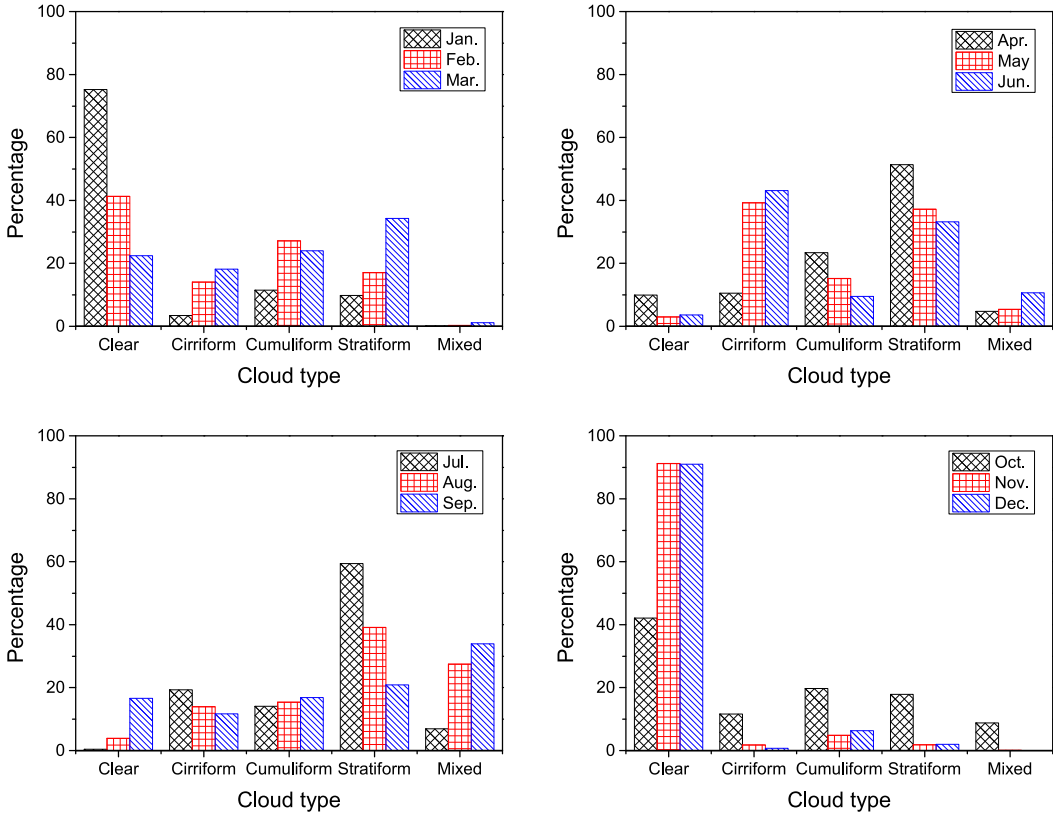

FIG. 4. The proportion of the five types of clouds by month.

March mainly consisted of four types of clouds: clear sky, cirriform, cumuliform, and stratiform, while the mixed clouds accounted for only a very small proportion. The difference is that clear sky accounted for the largest proportion in February, reaching 40%, whereas stratiform clouds have the largest proportion in March. Similarly, the stratiform clouds dominate in April, July, and August, and their proportions are more than 40% in these months. The proportion of the stratiform clouds in April and July is even more than 50%. Cirriform and stratiform clouds are the two most frequently occurring cloud types in May and June. In September, the probability of the appearance of the five types of clouds is relatively uniform.

We have counted the cloud types that have the highest frequency of each month, and the results are shown in Fig. 5. The cloud types in Shigatse also showed significant seasonal differences. The clear sky dominates in five months of the year, mainly occurring in autumn and winter. There are in total four months with the highest proportion of stratiform clouds. In September, mixed clouds appeared at a slightly higher frequency than other cloud types. The cloud type that has the highest percentage is cirriform cloud in May and June. Since the existing cloud detection algorithms have low recognition accuracy for cirrus clouds, this may lead to underestimation of cloud cover in May and June. The obvious turning point in May and June in Fig. 2 also indirectly illustrates this point. The cloud-type distribution in Shigatse is related to its climatic characteristics. The Shigatse region has a dry season in winter, with little

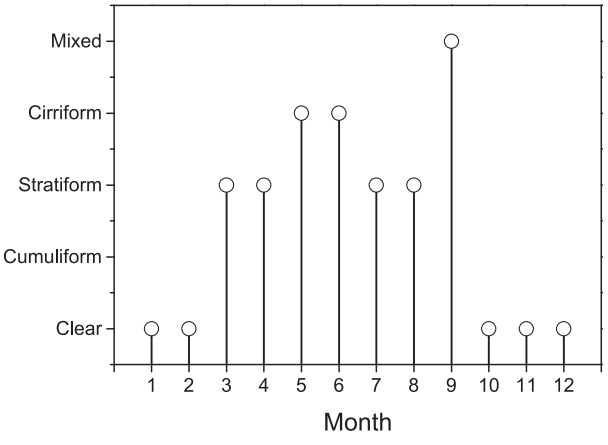

FIG. 5. The cloud type with the most frequent occurrence by month.

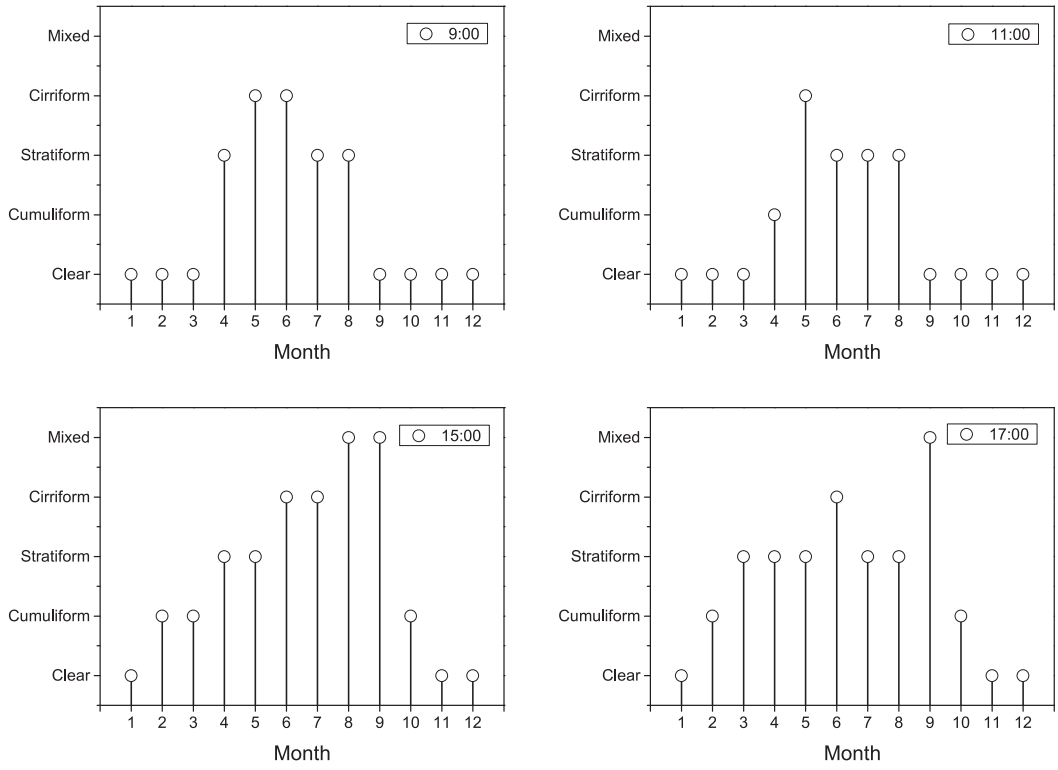

FIG. 6. The cloud type with the most frequent occurrence at four different times of day by month.

water vapor in the air, so it is mainly clear sky. Affected by the southwest monsoon in May and June, warm and humid airflow from the Indian Ocean rises along the TiP, causing more cirrus clouds because of topographic lifting. In July and August, the Shigatse region begins to enter the rainy season, and the water vapor resources in the atmosphere are extremely rich. Therefore, the cloud type also presents a state in which stratiform clouds dominate.

By counting the cloud-type information at the same time of the day, we can get the frequency of occurrence of a certain cloud type at that moment of each month. Figure 6 shows the cloud types with the highest occurrences at several typical moments in each month. At 0900 CST, there are in total seven months, mainly in autumn and winter, during which the probability of clear-sky appearance is the highest. At 1100 CST, the clear sky is still the most common sky type in the same seven months. At 1500 CST, the clear sky is dominant only in January, November, and December; the cloud type with the highest frequency is cumuliform cloud in February, March, and October; and the most common cloud type is mixed clouds in September. The most common cloud types for 1700 CST are very similar to those for 1500 CST in the same seven months except March, in which the most frequently occurring cloud type changed from cumuliform to stratiform cloud. The reason for this phenomenon may be that in winter and autumn the cloudiness in Shigatse is mainly affected by the daily radiation budget. The convection activity in the morning is relatively weak so that the cloudiness in the sky is very small. The convective activity begins to increase in the afternoon, which also leads to the increase of cloudiness in the sky and the abundance of cloud types. In other months, the combined effects of local convection and southwest warm and humid airflow have resulted in different cloud-type characteristics throughout the day. At several typical times in April, the cloud types that appeared the most are all stratiform clouds, except at 1100 CST for which the cloud with the highest frequency turned into cumuliform cloud. In the mornings of May, cirriform cloud is dominant, whereas in the afternoon the frequency of stratiform cloud appearance is the highest. In June, the cirriform cloud occupies the highest frequency at three typical times and at the other typical time (1100 CST) stratiform cloud is dominant. The situations in July and August are similar in that the most common cloud type is stratiform cloud at three typical times. The difference is that, at 1500 CST, the cirriform cloud occupies the dominant position in July whereas the mixed clouds have the advantage in August.

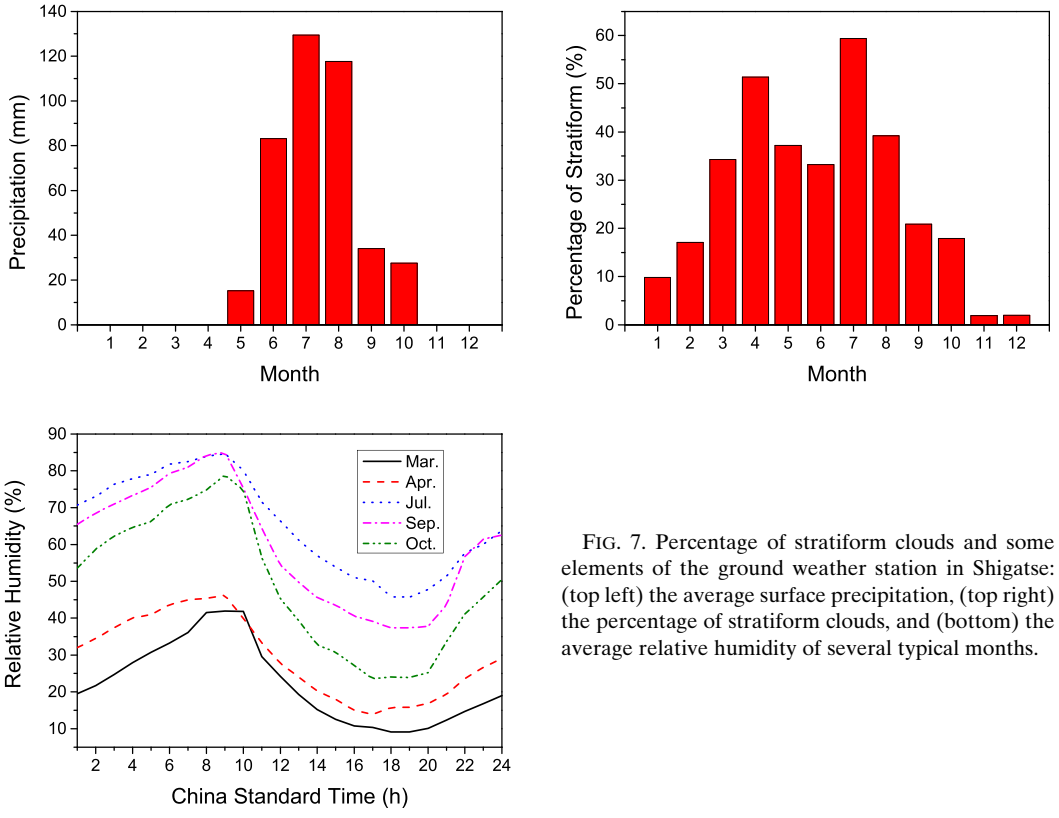

FIG. 7. Percentage of stratiform clouds and some elements of the ground weather station in Shigatse: (top left) the average surface precipitation, (top right) the percentage of stratiform clouds, and (bottom) the average relative humidity of several typical months.

c. Relationship between cloud and precipitation

In addition to analyzing the macroscopic features of monthly and diurnal variations of cloud cover and cloud type, we analyzed the relationship between precipitation and cloud cover and cloud type on the basis of the observation data of the ground weather station in Shigatse. The average surface precipitation in that area for two years is shown in the upper-left panel of Fig. 7, which demonstrates an obvious rainy and dry season. The precipitation in Shigatse mainly occurs from May to October, and there is almost no precipitation from November to the following April. The maximum cumulative precipitation occurs in July, and the precipitation in July and August accounted for more than 60% of the annual precipitation. From the monthly variation of cloud cover in Shigatse (Fig. 2), the cloud covers in July and August are also very high, and both their cloud cover values are over 60%. When we set up the TCIS database, we mentioned that the stratiform cloud type in this paper includes not only the real stratiform clouds but also some cumulonimbus clouds that cover the entire sky, which are the main cloud types that may cause the precipitation phenomenon. Therefore, we counted the percentage of stratiform clouds in each month, and the statistical results are shown in the upper-right panel of Fig. 7. It is obvious that the proportion of the stratiform clouds is the highest in July, which also corresponds to the largest amount of precipitation. On the other hand, we can also see that the proportion of stratiform clouds is very high from March to October, whereas precipitation mainly occurs from May to October. In particular, the proportion of stratiform clouds in March and April is significantly higher than that of September and October. In terms of monthly variation of cloud cover, the cloud cover in March and April is also obviously higher than that of September and October (see Fig. 2). To find out why there was no precipitation in March and April but there existed obvious rainfall in September and October is a key question. In general, surface precipitation is determined by the total precipitable water vapor in the atmosphere. If we have synchronous observation of precipitable water vapor (e.g., using ground-based microwave radiometers), we can explain this phenomenon better. Considering that there is a good correlation between the relative humidity on the ground and the total precipitable water vapor, we hope to give a possible explanation by comparing the average relative humidity of the ground in these months (see Fig. 7, bottom). It can be seen that at the same time the relative humidity of the

ground in September and October was evidently higher than that in March and April. It also shows that the precipitation on the ground is not only related to the coverage and type of clouds but also needs a favorable atmospheric environment, especially the water vapor resources in the air.

4. Conclusions

The TiP has an important impact on the global climate and water vapor cycle because of its special geographical environment. An in-depth analysis of macroattributes of the clouds in the TiP is an effective means of understanding its climatic characteristics. Although observation methods such as satellites and ground-based radars can perform some research on the macrocharacteristics of the clouds, their observation results need to be verified by ground-truth observations. Total-sky-imaging technology provides a feasible means for cloud automatic observation. With our self-developed TCI device, we conducted two years of continuous cloud observation and obtained a large number of total-sky images in the Shigatse region. The DTCA cloud detection algorithm and Caffe deep-learning cloud-classification method have been adopted to get cloud cover and cloud-type information for each total-sky image.

By analyzing all of the total-sky images, the statistical characteristics of cloud cover and cloud type in the Shigatse area can be summarized:

1) From the monthly variation of cloud cover in Shigatse, the cloud cover showed a significant seasonal distribution, which was mainly low cloud cover in autumn and winter and high cloud cover in summer and spring. There is also a great difference in the daily change of cloud cover in different months. Specifically, cloud cover is higher in the afternoon than in the morning in most months, and the cloud cover varies little all day from July to September. In all months, the average cloud cover in July is the largest, and the amount of cloudiness at each moment is basically fluctuating around 75%.
2) According to the frequency of occurrence of each cloud type in different months, the cloud types in Shigatse also presented evident seasonal differences. The clear sky is the most dominant sky type in five months, mainly in autumn and winter. Stratiform clouds accounted for the largest proportion in March, April, July, and August. The most likely cloud type in May and June is cirrus clouds. The frequency of various cloud types was relatively uniform in September, and the proportion of mixed clouds was only slightly higher.
3) The Shigatse region has a clear rainy and dry season, and its precipitation occurs mainly from May to October. The maximum cumulative precipitation appears in July, which also corresponds to the highest cloud cover and the highest ratio of stratiform clouds. Although the cloud amount and the proportion of stratiform clouds in March and April were higher than those in September and October, there was no precipitation in these two months. This result shows that the occurrence of precipitation is not only related to the cloud cover and cloud type but also needs the cooperation of a favorable atmospheric environment; the amount of water vapor in the air is especially an important factor.

Note that both stratus clouds and cumulonimbus clouds covering the sky are classified into stratiform clouds. This is because both cloud types are closely related to precipitation and the visible-imaging method that we adopted has difficulty in distinguishing between the two cloud types using only a single total-sky image. In the next stage, to get more accurate cloud-type classification, we can use two schemes to achieve it. The first option is to use the continuous changes of the clouds from multiple total-sky images to distinguish between stratus clouds and cumulonimbus clouds. The second option is to classify cumulonimbus clouds from stratus clouds by using the cloud-depth information, which can be obtained by combining the real-time atmospheric moisture profile information from the ground-based microwave radiometer profiler (Yang and Min 2018). Next, we will analyze the macroscopic characteristics of clouds in the TiP on the basis of satellite or ground-based radar observations, which will also help to better validate the conclusions of this study.

Acknowledgments. This work is partly funded by the National Natural Science Foundation of China (91537209 and 41675030), the National Key Scientific Instrument and Equipment Development Projects of China (2012YQ11020504), and the Basic Research Fund of Chinese Academy of Meteorological Sciences (2017Z003). We also thank Mr. Zhen Zhang for providing the Caffe deep-learning framework and total-sky cloud-classification parameters.

REFERENCES

Alonso, J., F. J. Batlles, G. López, and A. Ternero, 2014: Sky camera imagery processing based on a sky classification using radiometric data. *Energy*, **68**, 599–608, https://doi.org/10.1016/j.energy.2014.02.035.

Calbó, J., and J. Sabburg, 2008: Feature extraction from whole-sky ground-based images for cloud-type recognition. *J. Atmos.*

Oceanic Technol., **25**, 3–14, https://doi.org/10.1175/2007JTECHA959.1.

Chauvin, R., J. Nou, S. Thil, A. Traoré, and S. Grieu, 2015: Cloud detection methodology based on a sky-imaging system. *Energy Procedia*, **69**, 1970–1980, https://doi.org/10.1016/j.egypro.2015.03.198.

Duan, A., and G. Wu, 2006: Change of cloud amount and the climate warming on the Tibetan Plateau. *Geophys. Res. Lett.*, **33**, L22704, https://doi.org/10.1029/2006GL027946.

Gao, B.-C., P. Yang, G. Guo, S. K. Park, W. J. Wiscombe, and B. Chen, 2003: Measurements of water vapor and high clouds over the Tibetan Plateau with the *Terra* MODIS instrument. *IEEE Trans. Geosci. Remote Sens.*, **41**, 895–900, https://doi.org/10.1109/TGRS.2003.810704.

Garrett, T. J., and C. Zhao, 2006: Increased Arctic cloud longwave emissivity associated with pollution from mid-latitudes. *Nature*, **440**, 787–789, https://doi.org/10.1038/nature04636.

Ghonima, M. S., B. Urquhart, C. W. Chow, J. E. Shields, A. Cazorla, and J. Kleissl, 2012: A method for cloud detection and opacity classification based on ground based sky imagery. *Atmos. Meas. Tech.*, **5**, 2881–2892, https://doi.org/10.5194/amt-5-2881-2012.

Heinle, A., A. Macke, and A. Srivastav, 2010: Automatic cloud classification of whole sky images. *Atmos. Meas. Tech.*, **3**, 557–567, https://doi.org/10.5194/amt-3-557-2010.

Huang, J., and Coauthors, 2007: Summer dust aerosols detected from *CALIPSO* over the Tibetan Plateau. *Geophys. Res. Lett.*, **34**, L18805, https://doi.org/10.1029/2007GL029938.

Huo, J., and D. Lu, 2009: Cloud determination of all-sky images under low-visibility conditions. *J. Atmos. Oceanic Technol.*, **26**, 2172–2181, https://doi.org/10.1175/2009JTECHA1324.1.

——, and ——, 2012: Comparison of cloud cover from all-sky imager and meteorological observer. *J. Atmos. Oceanic Technol.*, **29**, 1093–1101, https://doi.org/10.1175/JTECH-D-11-00006.1.

Jia, Y., E. Shelhamer, J. Donahue, S. Karayev, J. Long, R. Girshick, S. Guadarrama, and T. Darrell, 2014: Caffe: Convolutional architecture for fast feature embedding. *Proc. 22nd ACM Int. Conf. on Multimedia*, Orlando, FL, Association for Computing Machinery, 675–678.

Johnson, R. W., T. L. Koehler, and J. E. Shields, 1988: A multistation set of whole sky imagers and a preliminary assessment of the emerging data base. *Proc. Cloud Impacts on DOD Operations and Systems Workshop*, Silver Spring, MD, Department of Defense, 159–162.

Kazantzidis, A., P. Tzoumanikas, A. F. Bais, S. Fotopoulos, and G. Economou, 2012: Cloud detection and classification with the use of whole-sky ground-based images. *Atmos. Res.*, **113**, 80–88, https://doi.org/10.1016/j.atmosres.2012.05.005.

Klebe, D. I., R. D. Blatherwick, and V. R. Morris, 2014: Ground-based all-sky mid-infrared and visible imager for purposes of characterizing cloud properties. *Atmos Meas. Tech.*, **7**, 637–645, https://doi.org/10.5194/amt-7-637-2014.

Li, Q., W. Lu, and J. Yang, 2011: A hybrid thresholding algorithm for cloud detection on ground-based color images. *J. Atmos. Oceanic Technol.*, **28**, 1286–1296, https://doi.org/10.1175/JTECH-D-11-00009.1.

——, Z. Zhang, W. Lu, J. Yang, Y. Ma, and W. Yao, 2016: From pixels to patches: A cloud classification method based on a bag of micro-structures. *Atmos. Meas. Tech.*, **9**, 753–764, https://doi.org/10.5194/amt-9-753-2016.

Li, Y., X. Liu, and B. Chen, 2006: Cloud type climatology over the Tibetan Plateau: A comparison of ISCCP and MODIS/*Terra* measurements with surface observations. *Geophys. Res. Lett.*, **33**, L17716, https://doi.org/10.1029/2006GL026890.

——, and M. Zhang, 2016: Cumulus over the Tibetan Plateau in the summer based on *CloudSat–CALIPSO* data. *J. Climate*, **29**, 1219–1230, https://doi.org/10.1175/JCLI-D-15-0492.1.

Liu, L., J. Zheng, Z. Ruan, Z. Cui, Z. Hu, S. Wu, G. Dai, and Y. Wu, 2015: Comprehensive radar observations of clouds and precipitation over the Tibetan Plateau and preliminary analysis of cloud properties. *J. Meteor. Res.*, **29**, 546–561, https://doi.org/10.1007/s13351-015-4208-6.

Long, C. N., 2010: Correcting for circumsolar and near-horizon errors in sky cover retrievals from sky images. *Open Atmos. Sci. J.*, **4**, 45–52, https://doi.org/10.2174/1874282301004010045.

——, and J. J. DeLuisi, 1998: Development of an automated hemispheric sky imager for cloud fraction retrievals. *Proc. 10th Symp. on Meteorological Observations and Instrumentation*, Phoenix, AZ, Amer. Meteor. Soc., 171–174.

——, J. M. Sabburg, J. Calbó, and D. Pagès, 2006: Retrieving cloud characteristics from ground-based daytime color all-sky images. *J. Atmos. Oceanic Technol.*, **23**, 633–652, https://doi.org/10.1175/JTECH1875.1.

Luo, Y., R. Zhang, W. Qian, Z. Luo, and X. Hu, 2011: Intercomparison of deep convection over the Tibetan Plateau–Asian monsoon region and subtropical North America in boreal summer using *CloudSat/CALIPSO* data. *J. Climate*, **24**, 2164–2177, https://doi.org/10.1175/2010JCLI4032.1.

Neto, S. L. M., A. von Wangenheim, E. B. Pereira, and E. Comunello, 2010: The use of Euclidean geometric distance on RGB color space for the classification of sky and cloud patterns. *J. Atmos. Oceanic Technol.*, **27**, 1504–1517, https://doi.org/10.1175/2010JTECHA1353.1.

Shankar, D., P. N. Vinayachandran, and A. S. Unnikrishnan, 2002: The monsoon current in the north Indian Ocean. *Prog. Oceanogr.*, **52**, 63–120, https://doi.org/10.1016/S0079-6611(02)00024-1.

Shields, J. E., M. E. Karr, R. W. Johnson, and A. R. Burden, 2013: Day/night whole sky imagers for 24-h cloud and sky assessment: History and overview. *Appl. Opt.*, **52**, 1605–1616, https://doi.org/10.1364/AO.52.001605.

Song, X., X. Zhai, L. Liu, and S. Wu, 2017: Lidar and ceilometer observations and comparisons of atmospheric cloud structure at Nagqu of Tibetan Plateau in 2014 summer. *Atmosphere*, **8**, 9, https://doi.org/10.3390/atmos8010009.

Souza-Echer, M. P., E. B. Pereira, L. S. Bins, and M. A. R. Andrade, 2006: A simple method for the assessment of the cloud cover state in high-latitude regions by a ground-based digital camera. *J. Atmos. Oceanic Technol.*, **23**, 437–447, https://doi.org/10.1175/JTECH1833.1.

Stephens, G. L., 2005: Cloud feedbacks in the climate system: A critical review. *J. Climate*, **18**, 237–273, https://doi.org/10.1175/JCLI-3243.1.

Wang, C., H. Shi, H. Hu, Y. Wang, and B. Xi, 2015: Properties of cloud and precipitation over the Tibetan Plateau. *Adv. Atmos. Sci.*, **32**, 1504–1516, https://doi.org/10.1007/s00376-015-4254-0.

Wang, S., W. He, H. Chen, J. Bian, and Z. Wang, 2016: Statistics of cloud heights over the Tibetan Plateau and its surrounding region derived from CloudSat data. *Sci. Cold Arid Reg.*, **8**, 72–81, https://doi.org/10.3724/SP.J.1226.2016.00072.

Yabuki, M., M. Shiobara, K. Nishinaka, and M. Kuji, 2014: Development of a cloud detection method from whole-sky color images. *Polar Sci.*, **8**, 315–326, https://doi.org/10.1016/j.polar.2014.07.004.

Yamashita, M., and M. Yoshimura, 2012: Ground-based cloud observation for satellite-based cloud discrimination and its validation. *Int. Archives of the Photogrammetry, Remote*

Sensing and Spatial Information Sciences, Vol. 39-B8, Melbourne, Australia, International Society for Photogrammetry and Remote Sensing, 137–140, https://www.int-arch-photogramm-remote-sens-spatial-inf-sci.net/XXXIX-B8/137/2012/isprsarchives-XXXIX-B8-137-2012.pdf.

Yang, H., B. Kurtz, D. Nguyen, B. Urquhart, C. W. Chow, M. Ghonima, and J. Kleissl, 2014: Solar irradiance forecasting using a ground-based sky imager developed at UC San Diego. *Sol. Energy*, **103**, 502–524, https://doi.org/10.1016/j.solener.2014.02.044.

Yang, J., and Q. Min, 2018: Retrieval of atmospheric profiles in the New York State Mesonet using one-dimensional variational algorithm. *J. Geophys. Res. Atmos.*, **123**, https://doi.org/10.1029/2018JD028272, in press.

——, W. Lu, Y. Ma, and W. Yao, 2012: An automated cirrus cloud detection method for a ground-based cloud image. *J. Atmos. Oceanic Technol.*, **29**, 527–537, https://doi.org/10.1175/JTECH-D-11-00002.1.

——, Q. Min, W. Lu, W. Yao, Y. Ma, J. Du, T. Lu, and G. Liu, 2015: An automated cloud detection method based on the green channel of total-sky visible images. *Atmos. Meas. Tech.*, **8**, 4671–4679, https://doi.org/10.5194/amt-8-4671-2015.

——, ——, ——, Y. Ma, W. Yao, T. Lu, J. Du, and G. Liu, 2016: A total sky cloud detection method using real clear sky background. *Atmos. Meas. Tech.*, **9**, 587–597, https://doi.org/10.5194/amt-9-587-2016.

——, ——, ——, ——, ——, and ——, 2017: An RGB channel operation for removal of the difference of atmospheric scattering and its application on total sky cloud detection. *Atmos. Meas. Tech.*, **10**, 1191–1201, https://doi.org/10.5194/amt-10-1191-2017.

You, Q., Y. Jiao, H. Lin, J. Min, S. Kang, G. Ren, and X. Meng, 2014: Comparison of NCEP/NCAR and ERA-40 total cloud cover with surface observations over the Tibetan Plateau. *Int. J. Climatol.*, **34**, 2529–2537, https://doi.org/10.1002/joc.3852.

Zhang, X., L. Peng, D. Zheng, and J. Tao, 2008: Cloudiness variations over the Qinghai-Tibetan Plateau during 1971–2004. *J. Geogr. Sci.*, **18**, 142–154, https://doi.org/10.1007/s11442-008-0142-1.

Zhang, Z., 2017: The study of all-sky cloud classification based on deep learning (in Chinese). M.S. Thesis, School of Computer and Information Technology, Beijing Jiaotong University, 57 pp.

Zhao, C., S. A. Klein, S. Xie, X. Liu, J. S. Boyle, and Y. Zhang, 2012: Aerosol first indirect effects on non-precipitating low-level liquid cloud properties as simulated by CAM5 at ARM sites. *Geophys. Res. Lett.*, **39**, L08806, https://doi.org/10.1029/2012GL051213.

——, L. Liu, Q. Wang, Y. Qiu, W. Wang, Y. Wang, and T. Fan, 2016: Toward understanding the properties of high ice clouds at the Naqu site over the Tibetan Plateau using ground-based active remote sensing measurements obtained during a short period in July 2014. *J. Appl. Meteor. Climatol.*, **55**, 2493–2507, https://doi.org/10.1175/JAMC-D-16-0038.1.

——, ——, ——, ——, Y. Wang, and X. Wu, 2017: MMCR-based characteristic properties of non-precipitating cloud liquid droplets at Naqu site over Tibetan Plateau in July 2014. *Atmos. Res.*, **190**, 68–76, https://doi.org/10.1016/j.atmosres.2017.02.002.